JGR Oceans

RESEARCH ARTICLE
10.1029/2022JC018904

Thermocline Salinity Minima Due To Wind-Driven Differential Advection

Evridiki Chrysagi[1], N. Berkay Basdurak[1,2], Lars Umlauf[1], Ulf Gräwe[1], and Hans Burchard[1]

[1]Leibniz Institute for Baltic Sea Research, Warnemünde, Germany, [2]Institute of Marine Sciences, Middle East Technical University, Erdemli, Turkey

Key Points:

- Observations collected in the central Baltic Sea during summer indicate patches of distinct salinity minima in the thermocline region
- Realistic high-resolution simulations are used to explore the origin of the salinity minima and to identify the hotspots of their genesis
- Lateral surface salinity gradients interacting with wind-induced differential advection are shown to generate most of the inversions

Supporting Information:

Supporting Information may be found in the online version of this article.

Correspondence to:

E. Chrysagi,
evridiki.chrysagi@io-warnemuende.de

Citation:

Chrysagi, E., Basdurak, N. B., Umlauf, L., Gräwe, U., & Burchard, H. (2022). Thermocline salinity minima due to wind-driven differential advection. *Journal of Geophysical Research: Oceans*, *127*, e2022JC018904. https://doi.org/10.1029/2022JC018904

Received 27 MAY 2022
Accepted 13 OCT 2022

Abstract Observations from the global ocean have long confirmed the ubiquity of thermohaline inversions in the upper ocean, often accompanied by a clear signal in biogeochemical properties. Their emergence has been linked to different processes such as double diffusion, mesoscale stirring, frontal subduction, and the recently discussed submesoscale features. This study uses the central Baltic Sea as a natural laboratory to explore the formation of salinity inversions in the thermocline region during summer. We use realistic high-resolution simulations complemented by field observations to identify the dominant generation mechanism and potential hotspots of their emergence. We propose that the strongly stratified thermocline can host distinct salinity minima during summer conditions resulting primarily from the interaction between lateral surface salinity gradients and wind-induced differential advection. Since this is a generic mechanism, such salinity inversions can likely constitute a typical feature of the upper ocean in regions with distinct thermoclines and shallow mixed layers.

Plain Language Summary The upper ocean is characterized by a well-mixed surface layer, below which temperature decreases rapidly with depth, forming the so-called thermocline region. A corresponding salinity increase with depth is typically anticipated for stable density stratification to occur. Temperature and salinity inversions can, however, emerge in the upper ocean. Such thermohaline inversions have been observed in different regions of the world's oceans, and various mechanisms have been proposed to explain their generation. Here, the central basin of the Baltic Sea is used as a natural laboratory to explore the formation of distinct salinity minima in the thermocline region during summer conditions. Using high-resolution numerical simulations and measurements from a field campaign, we show that inversions are abundant and can emerge throughout the entire basin. They increase with increasing wind speeds and concentrate mainly in regions with strong lateral salinity differences. We propose that thermocline salinity minima can occur during summer when the wind transports saltier water over less saline surface waters. This is a generic mechanism that can therefore be responsible for the formation of the salinity inversions observed worldwide in areas with distinct thermoclines and shallow mixed layers.

1. Introduction

Density-compensated inversions in oceanic salinity and temperature profiles are frequently observed in the ocean. Thermal inversions, compensated by stable salinity stratification, were reported, for example, in the Pacific Ocean at frontal zones and were ascribed to lateral advection (Roden, 1964; Ueno et al., 2007). Temperature-compensated salinity inversions were observed in the Timor Sea and shown to be associated with sheared lateral advection in the presence of lateral temperature and salinity gradients (Stommel & Fedorov, 1967). These features are important in understanding the mean turbulent transport of heat and salt in the clines of the ocean, as noted by Stommel and Fedorov (1967).

Inversions may also be indicative of thermohaline interleaving (Ruddick & Richards, 2003), which can cause significant, self-driven, lateral mixing of heat, salt, and momentum, using the available thermoclinic potential energy (Woods et al., 1986). Apart from double-diffusion (Ruddick & Richards, 2003), other processes triggering salinity and temperature inversions include: mesoscale eddy-stirring (Pietri et al., 2013; Smith & Ferrari, 2009), and frontal subduction in regions with submesoscale activity, as evidenced by various observational studies (e.g., Hosegood et al., 2013; Thomsen et al., 2016). Especially the latter are mainly bound to the upper ocean, below the mixed layer (ML).

Sites like the North Pacific Subtropical Frontal Zone (Hosegood et al., 2013), the Peruvian (Pietri et al., 2013; Thomsen et al., 2016), and the Benguela upwelling systems (Armstrong et al., 1987) also show observational evidence for salinity inversions in the upper ocean. There, the inversions were often associated with biogeochemical signatures driven by frontal and submesoscale dynamics. Similarly, smaller upwelling systems in the Baltic Sea have shown salinity inversions in the thermocline (Lass et al., 2010; Lips et al., 2016).

In the upper MLs of the Baltic Sea, Burchard et al. (2017) identified offshore Ekman transport, under significant surface warming, as the primary source of inversions, away from the upwelling region. They argued that inversions result from an advective modification of the surface-layer thermohaline properties rather than a modification of the inversion layer itself. Their findings contrast previous studies on subduction and intrusions of different water masses into the intrusion layer. However, Burchard et al. (2017) (a) linked these inversions to upwelling events and (b) used a simple box model that ignored spatial variations arising, for example, from mesoscale and submesoscale surface-layer structures and spatial inhomogeneities in the wind field. Thus, although their study provided a first explanation for the origin of the thermocline salinity anomalies in the vicinity of upwelling fronts, the underlying dynamics in the offshore regions were not fully explored.

Here, we aim to extend their study by investigating the conditions that trigger thermocline salinity inversions in a broader context. To explore these globally relevant oceanic features we use the central Baltic Sea, characterized by sharp lateral salinity gradients and a rich submesoscale activity (Chrysagi et al., 2021), as a natural laboratory. With a realistic numerical model complemented by field observations, we show that salinity inversions are ubiquitous in the upper part of the water column just below the ML, arising not just in the upwelling regions but throughout the entire basin. To explain their emergence, we propose a simple yet efficient mechanism that may be of global relevance.

After introducing our observations and the numerical model in Section 2, our hypothesis and the theoretical framework for the generation of the salinity inversions are presented in Section 3. In Section 4, we first demonstrate the spatial distribution of the salinity minima and their abundance in the central Baltic Sea. Then, additional analysis is conducted to evaluate our hypothesis that upper-ocean salinity inversions emerge primarily from the interaction between the horizontal surface salinity gradients and wind-induced differential advection in regions with distinct thermoclines. The results are briefly summarized and discussed in Section 5.

2. Numerical Model and Observations

2.1. Field Observations

High-resolution measurements were collected during a field campaign (green box in Figure 1b) in the Eastern Gotland Basin from 7 to 15 July 2012 (for details see Burchard et al., 2017). Here, the acquired measurements serve mainly as a motivation thus only a single conductivity-temperature-depth (CTD) chain transect is used (magenta line in Figure 1b). The CTD chain was towed by R/V Elisabeth Mann Borgese and was equipped with multiple sensor fins, providing data with a mean vertical resolution of around 1 m. The horizontal resolution of this ∼19 km transect is 6 m. The transect was sampled on 12 July after the onset of an upwelling episode. Temperature, salinity, and density profiles of the upper 50 m of the water column are shown in Figures 1c–1e. Although the surface boundary layer was stably stratified along the transect, salinity minima emerged at depths between 20 and 30 m, corresponding to the thermocline layer.

2.2. Model Setup

We conducted realistic high-resolution simulations using the General Estuarine and Transport Model (Burchard & Bolding, 2002) to explore the driving mechanism of the observed thermocline salinity anomalies and to detect potential spatial hotspots of their formation. A detailed model description is provided in Chrysagi et al. (2021), where a similar configuration was used to investigate the submesoscale dynamics in the central Baltic Sea. Thus, we present only the most relevant model features here. The model domain spans from 15.5° to 24.0°E and from 54.2° to 60.6°N (Figure 1a). The horizontal grid size varies between 500 and 600 m, which is submesoscale resolving (Chrysagi et al., 2021). We utilized 100 adaptive vertical layers (Burchard & Beckers, 2004; Hofmeister et al., 2010), where the upper 50 layers were limited to a maximum layer thickness of ∼1 m to resolve the upper-ocean dynamics correctly.

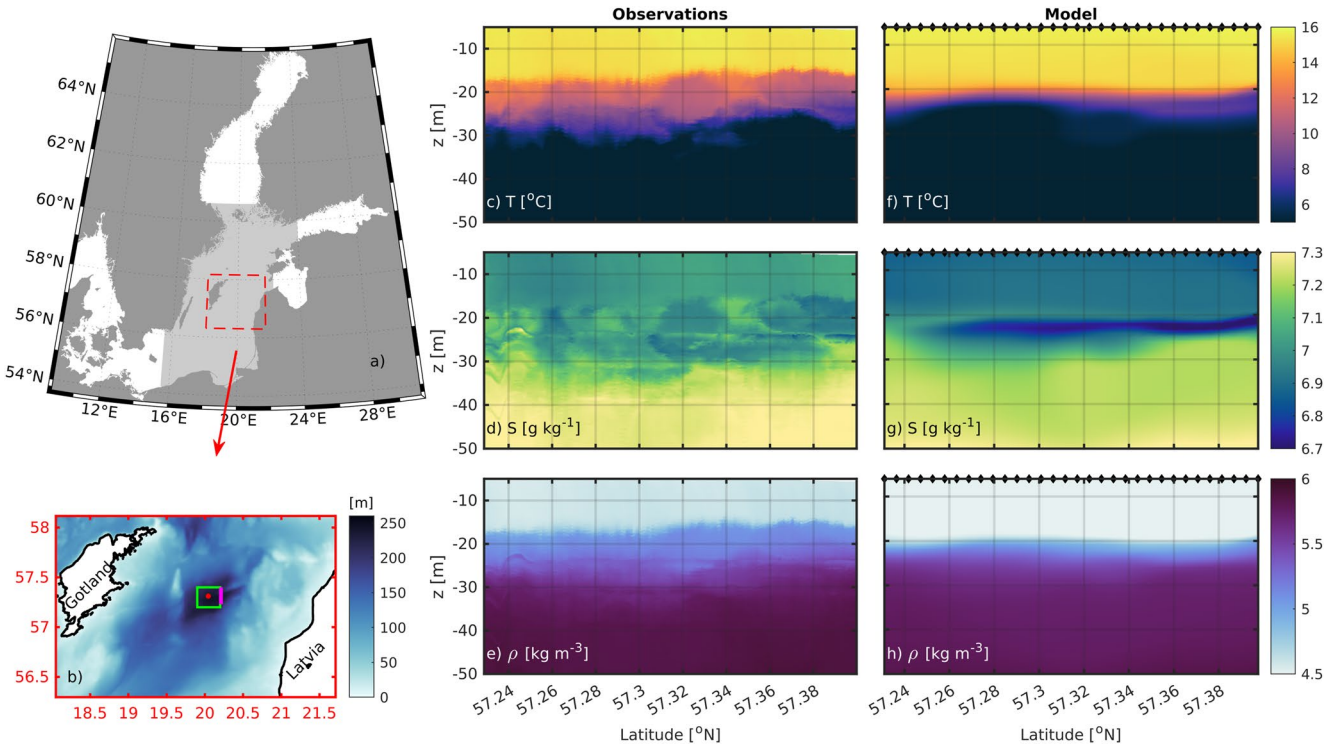

Figure 1. (a) Model domain (Baltic Proper), shaded in light gray, along with the study area (red box). (b) Bathymetry of the study area (Eastern Gotland Basin) with the red dot marking the monitoring station TF271, the magenta line showing the conductivity-temperature-depth (CTD) chain transect, and the green box indicating the observational area. Vertical sections of observed (c–e) and modeled (f–h) temperature, salinity, and density fields. The CTD chain transect data were sampled on 12 July 2012; the model transect is a snapshot of the same day at 10:00 UTC. Black markers in (f–h) indicate the model resolution.

The horizontal viscosity was parameterized according to Smagorinsky (1963) using a Smagorinsky constant of 0.28 and a turbulent Prandtl number of 2.0 for tracers. Vertical mixing was parameterized through a two-equation k-ε turbulence model with an algebraic second-moment closure (Umlauf & Burchard, 2005). To mimic the unresolved part of the internal wave spectrum, we prescribed a background turbulent kinetic energy level of $k_{\min} = 5 \times 10^{-8}$ m^2 s^{-2} (see also Holtermann et al., 2014). Moreover, we imposed a stratification limitation of the turbulent length scale by the Ozmidov scale as proposed by Galperin et al. (1988). The atmospheric forcing was taken from the Climate Forecast System Reanalysis simulations of Saha et al. (2010) with a spatio-temporal resolution of 1/5° and 1 hr respectively. The lateral boundary conditions were extracted from a one nautical mile Baltic Sea model (Gräwe et al., 2019). The simulation period is from 1 January to 1 August 2012.

2.3. Model Validation

For validating the model, we used satellite data and a variety of field observations. Here, only typical examples are shown, comparing the model results with the observations. Satellite images and the model results of surface temperature are in good agreement (Figure 2). Minor discrepancies are found in the upwelling areas, that is, along the Swedish coast, the Öland and Gotland islands; this can be attributed to the atmospheric forcing. Sensitivity experiments using atmospheric data sets with different spatio-temporal resolutions, showed inconsistencies not just in the lateral extent and the strength of the upwelling cells but also in the overall surface temperature structure. The discrepancy around Gotland island can also be due to the model failing to reproduce the propagation properties of coastal trapped Kelvin waves; these waves diminish the upwelling along the east coast and restrict the upwelling region at the southernmost tip of the island (Fennel et al., 2010).

Likewise, the use of FerryBox data for the months June and July show that the simulated temperature closely matches the observed one (Figure 3 left column). The model captures also the overall surface salinity structure and the higher salinity waters of the southwestern Baltic Proper advecting into the study area (Figure 3 right column). There is, however, a discrepancy in the surface salinity field at the open boundary of the model (~23°E

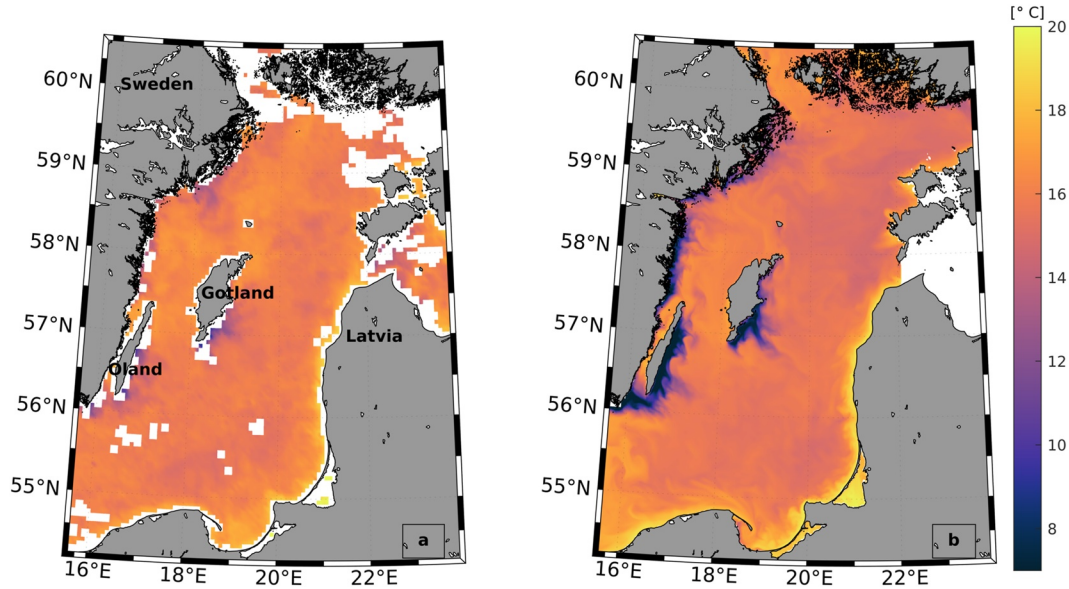

Figure 2. Sea surface temperature (SST) in the Baltic Proper from (a) observations and from (b) the numerical model. The observed SST is a satellite image obtained from the Federal Maritime and Hydrographic Agency of Germany (BSH). White areas on (a) indicate missing data due to cloud cover. Both panels are daily averaged fields for 16 July 2012.

and 59.5°N), close to the Gulf of Finland; the model overestimates the relatively fresh water tongue that is visible in the measurements. To explore the model's capability in reproducing the vertical structure of the water column, temperature and salinity profiles from the HELCOM standard monitoring program were used (http://www.helcom.fi). An example comparing observed and simulated temperature and salinity profiles in the center of the basin (station TF271, marked with a red dot in Figure 1) is illustrated in Figure 4. For the upper 40 m, which is the focus of this study, the model is in good agreement with the observations. Below that, minor deviations are found mainly in the representation of the remaining cold "winter water" whereas, in the deeper parts of the water column, the model is found to be slightly colder and more saline than the measurements.

We also compared simulated profiles of temperature, salinity, and density to the CTD-chain transect shown in Figure 1b. While the model is consistent with the observations in capturing the salinity inversions for the same day and location, their structure is more elongated and less patchy than the observed one. This is most likely due to the considerably lower horizontal resolution in the model (600 m) compared to the measurements (6 m). Moreover, it should be noted that the simulated thermocline is substantially narrower than the observed one (Figure 1c vs. Figure 1f). Regardless of the exact inversion structure, the vertical difference between the ML salinity and the thermocline salinity, which is crucial for our analysis (see Section 3), is in both cases ∼0.2 g kg^{-1}. Stable stratification is preserved (Figures 1e and 1h) even in the presence of inversions. Here, the salinity minima occur in the thermocline layer, where a stable temperature gradient overcompensates an unstable salinity gradient.

3. Theory

Further measurements collected during the survey (not shown) suggest that salinity inversions increase with increasing wind speeds. Processes, such as wind-driven submesoscale subduction due to intense buoyancy loss (Hosegood et al., 2013) and down-front winds (Thomas & Lee, 2005) or frontal-subduction due to strong ageostrophic circulation (Pietri et al., 2013) cannot be the primary generating mechanism here. This is evidenced by submesoscale features that, for our study period, seem to emerge only during the upwelling event in localized regions, whereas inversions are visible during the entire period and in different areas (see Section 4). Submesoscales may, however, contribute locally to the emergence of inversions. Moreover, thermohaline interleaving, which plays a vital role in the Baltic Sea, is an unlikely reason for the inversions because (a) it is not directly related to variations in the wind speed and (b) it usually occurs in deeper layers in the Gotland Basin (e.g., Kuzmina et al., 2005).

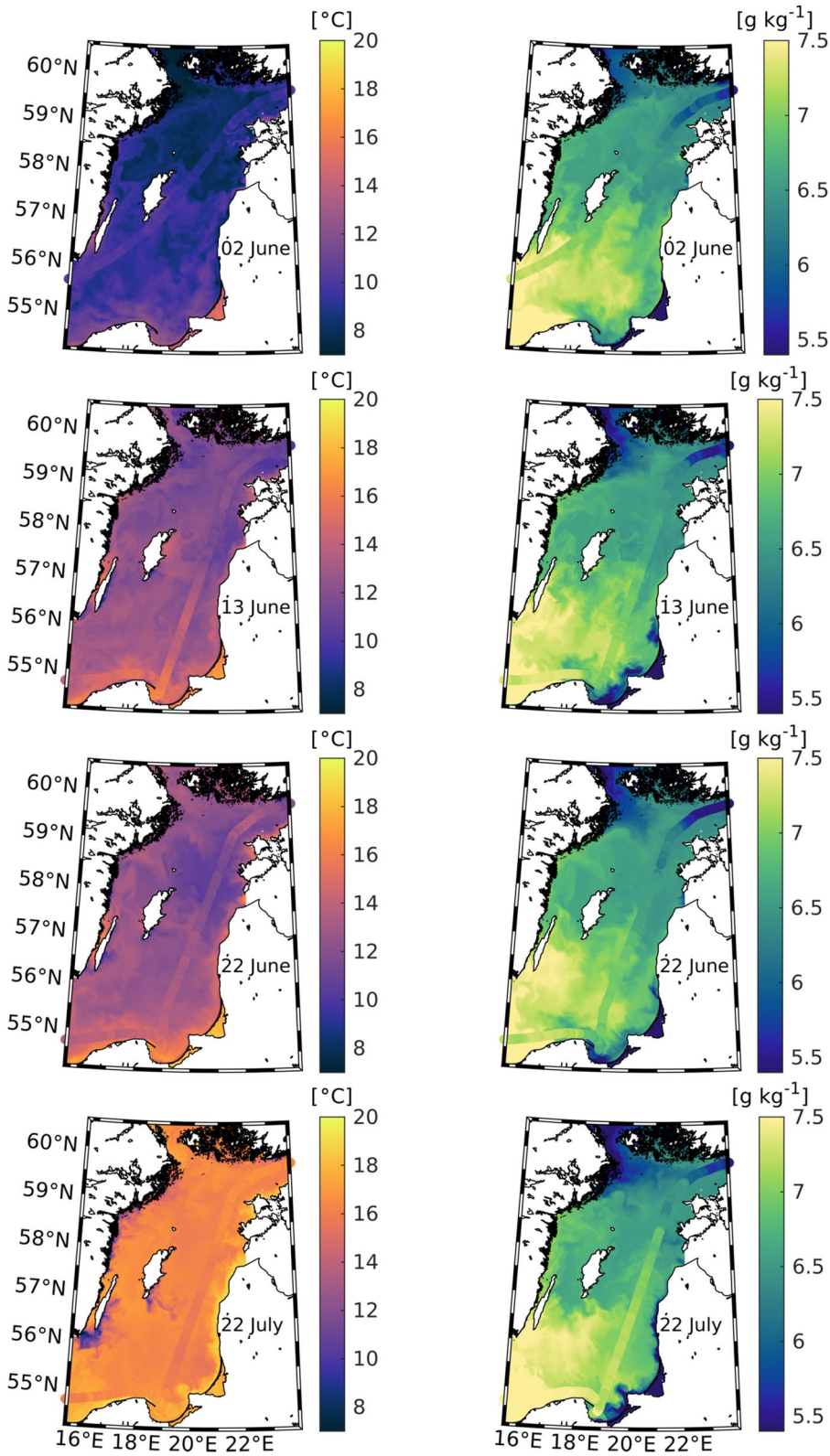

Figure 3. Sea surface temperature (left column) and salinity (right column) fields in the Baltic Proper. The FerryBox data, collected by a thermosalinograph mounted on a ferry, are drawn as continuous circles along the cruise tracks on top of the model output.

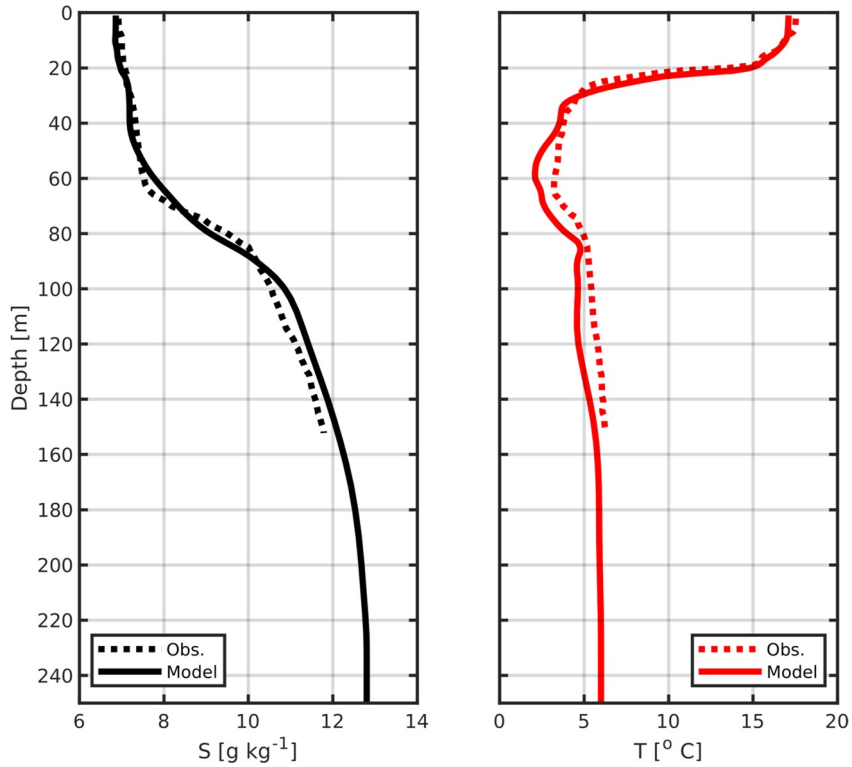

Figure 4. Vertical salinity (black) and temperature (red) profiles from observations (dashed line) and the numerical model (continuous line) at the monitoring station TF271 (marked in Figure 1). All fields concern snapshots after the end of the field campaign (30 July 13:00 UTC).

We, therefore, hypothesize that wind-induced differential advection is, to a large extent, instrumental in generating salinity minima by transporting more saline water on top of less saline water (see Figure 5). To test our hypothesis, we diagnose the amount of differential advection by employing the horizontal salinity advection equation:

$$\partial_t S + \boldsymbol{u} \cdot \nabla S = 0, \tag{1}$$

where ∂_t is the partial time derivative, S is the salinity, $\boldsymbol{u}$ is the horizontal velocity vector, and ∇ is the gradient operator. Assuming a ML with thickness h and ignoring vertical covariance between velocity and salinity

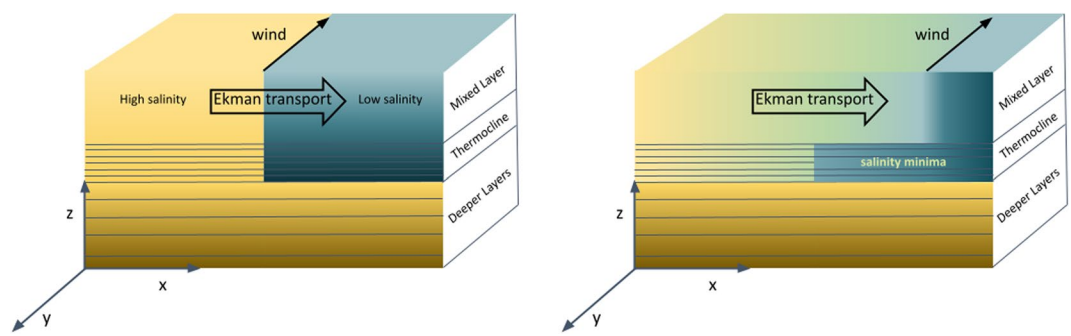

Figure 5. Generation of salinity minima due to wind-driven differential advection. As the wind blows on top of a preexisting horizontal salinity gradient, it induces Ekman transport. If the lateral salinity gradient is favorably aligned to the Ekman transport, saltier waters will move on top of less saline waters. As a result, salinity minima will emerge in the thermocline region, just below the mixed layer (right). This generation mechanism concerns summer conditions, when strongly stratified thermoclines that can host the salinity minima develop, and salinity behaves almost as a passive tracer. A movie illustrating this process through numerical simulations is also provided in Supporting Information S1.

gradients (due to the assumption of a well-mixed surface layer with small vertical gradients in velocity and salinity), vertical averaging of Equation 1 over the ML gives:

$$\partial_t \bar{S} + \bar{\boldsymbol{u}} \cdot \nabla \bar{S} = 0, \tag{2}$$

where an overbar denotes a vertical average. To construct a robust analysis method, we ignore motion and temporal salinity changes in the thermocline on time scales of 1 day. We reformulated this to:

$$\partial_t \Delta\bar{S} + \bar{\boldsymbol{u}} \cdot \nabla \bar{S} = 0, \tag{3}$$

where $\Delta\bar{S}$ is the difference between the vertically integrated ML salinity and the salinity in the thermocline region. After introducing temporal averaging as:

$$\langle X(t) \rangle = \frac{1}{T} \int_{t-T/2}^{t+T/2} X(\tau) \mathrm{d}\tau, \tag{4}$$

with the averaging interval $T > 0$, where T is the time, we obtain:

$$\Delta\bar{S} = \Delta\bar{S}_{init} - T \left\langle \bar{\boldsymbol{u}} \cdot \nabla \bar{S} \right\rangle, \tag{5}$$

where $\Delta\bar{S}_{init}$ is the ML to thermocline salinity difference at the beginning of the averaging interval and $\Delta\bar{S}$ is the value at the end. With this, the condition for a salinity inversion, that is, $\Delta\bar{S} > 0$ (unstable salinity stratification), is:

$$\left\langle \bar{\boldsymbol{u}} \cdot \nabla \bar{S} \right\rangle < \frac{\Delta\bar{S}_{init}}{T}. \tag{6}$$

To interpret Equation 6, we start with the assumption of a negative $\Delta\bar{S}$ (stable salinity stratification). The time it takes for a negative straining term $\left\langle \bar{\boldsymbol{u}} \cdot \nabla \bar{S} \right\rangle$, to yield unstable salinity stratification is:

$$T > \frac{\Delta\bar{S}_{init}}{\left\langle \bar{\boldsymbol{u}} \cdot \nabla \bar{S} \right\rangle} > 0. \tag{7}$$

Equation 6 suggests that the wind plays a dual role in the inversions depending on its direction with respect to the lateral salinity gradients. It can enhance the minima when favorably aligned by transporting more saline waters above less saline waters.

Assuming that salinity generally increases with depth, salinity minima are defined here by a positive vertical difference between the ML salinity $\left(\bar{S}_{ml}\right)$ and the salinity in the thermocline region $\left(\bar{S}_{th}\right)$, that is, $\Delta\bar{S} = \bar{S}_{ml} - \bar{S}_{th} > 0$ (overbar denotes vertical averaging). Higher $\Delta\bar{S}$ values thus indicate stronger inversions. To determine the thermocline region, the method provided by Chu and Fan (2019) is used. For diagnosing the mixed layer depth (MLD), we use a vertical density threshold of 0.03 kg m^{-3} (i.e., $\Delta\rho = \rho|_z - \rho|_{z=0} > 0.03$ kg m^{-3}) as proposed by de Boyer Montégut et al. (2004) and applied for the same region in Chrysagi et al. (2021). Based on the above, a detection algorithm for the inversions was generated. Note here that sensitivity analysis using higher threshold values for the definition of the MLD (e.g., Onken et al., 2020) showed that the detection algorithm is only weakly sensitive to the choice of the threshold value.

4. Results and Analysis

Atmospheric conditions (Figure 6a) in the study area were relatively calm in July 2012 except during the field campaign (7–15 July 2012), when pronounced southwesterly winds were observed. As shown below, this event created an extended coastal upwelling cell near the island of Gotland and increased the number of inversions. Before the onset of the upwelling on 8 July, the surface temperature was relatively uniform over the basin, with slightly higher values nearby the coast of Latvia and lower values at the northern part of the domain (Figure 6d). The surface salinity structure showed a distinct northeast-southwest gradient, with the brackish northern waters surrounding the higher salinity water masses in the center of the basin (Figure 6e). Strong lateral salinity gradients appeared everywhere in the basin; as outlined in Section 3, significant salinity gradients are a key factor in our hypothesis.

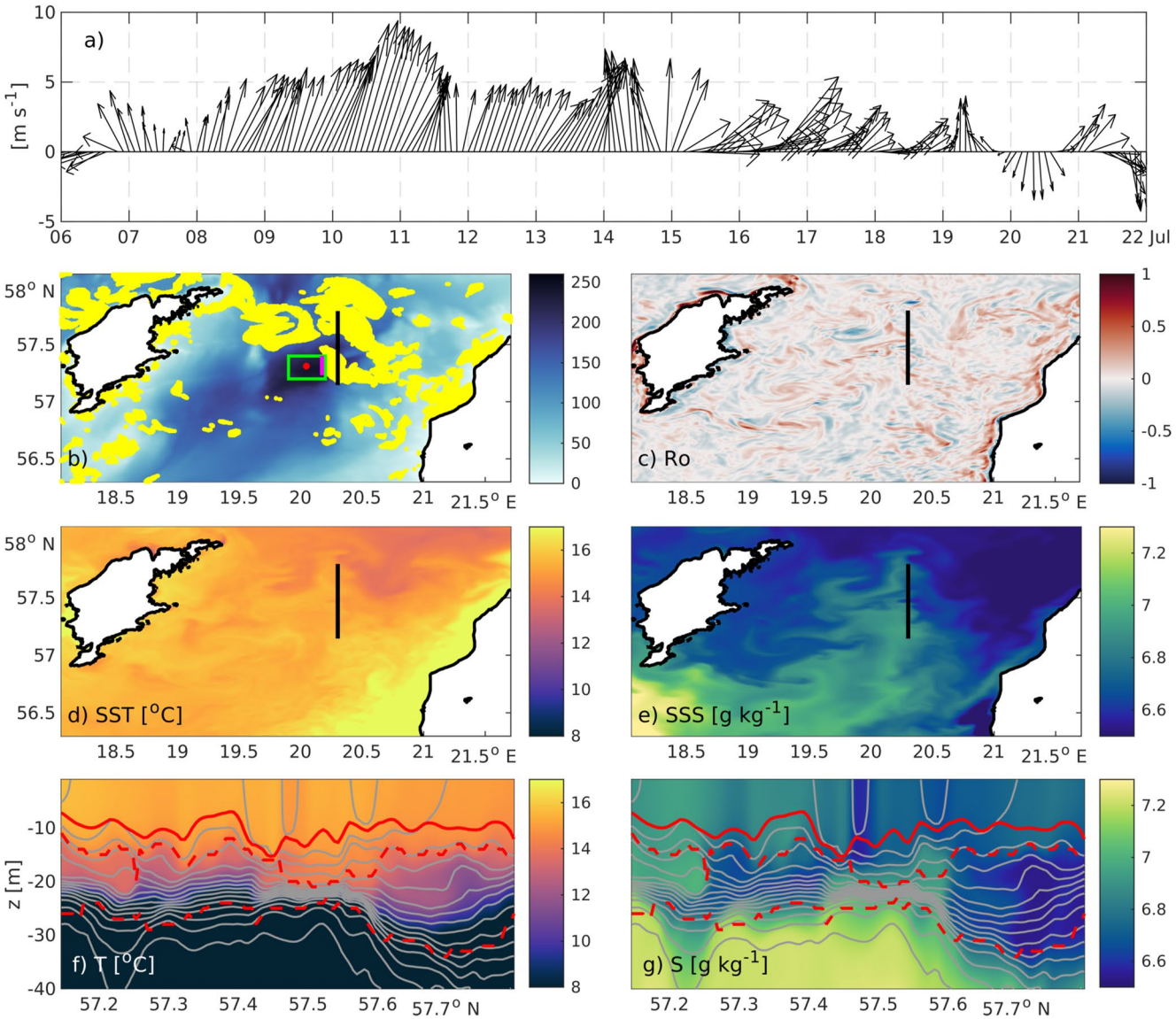

Figure 6. (a) Basin-averaged wind speed and direction. (b) Bathymetry of the study area and salinity inversions (yellow dots) as identified by the detection algorithm. The green box illustrates the region where shipboard measurements were collected, the magenta line indicates the location of the conductivity-temperature-depth (CTD) chain transect shown in Figures 1c–1e, and the red dot demonstrates the position of the monitoring station TF271. (c) Rossby number (Ro), (d) sea surface temperature (SST), and (e) sea surface salinity (SSS). Vertical sections of (f) temperature and (g) salinity along the black line shown in panels (d and e) respectively. Gray contours in both panels denote isopycnals at 0.1 kg m^{-3} intervals, the solid red lines show the mixed layer depth; upper and lower boundaries of the thermocline are shown as dashed red lines. Panels (b–g) are snapshots before the onset of the upwelling event, on 08 July 16:00 UTC.

Smaller-scale features like fronts and filaments, with a clear signal in the surface salinity field, developed in the study area. Inside these features the Rossby number, defined here as the relative vorticity ζ normalized by the Coriolis frequency f that is, Ro = ζ/f, showed relatively low values (Figure 6c), indicative of weak submesoscale activity. However, as shown below, a plethora of submesoscale structures with Ro $\sim \mathcal{O}(1)$ emerged locally during the upwelling event when the lateral surface density gradients intensified. Focusing on the vertical structure, a meridional temperature transect at the center of the basin indicates a relatively shallow ML (continuous red line in Figure 6f). A broad thermocline bounds the ML with a thickness of around 10–15 m (dashed lines in Figure 6f). Inside the thermocline region, patches of distinct salinity minima appear with vertical salinity differences between the thermocline and the overlying surface waters reaching up to 0.2–0.3 g kg^{-1} (Figure 6g). Those features are the focus of this study.

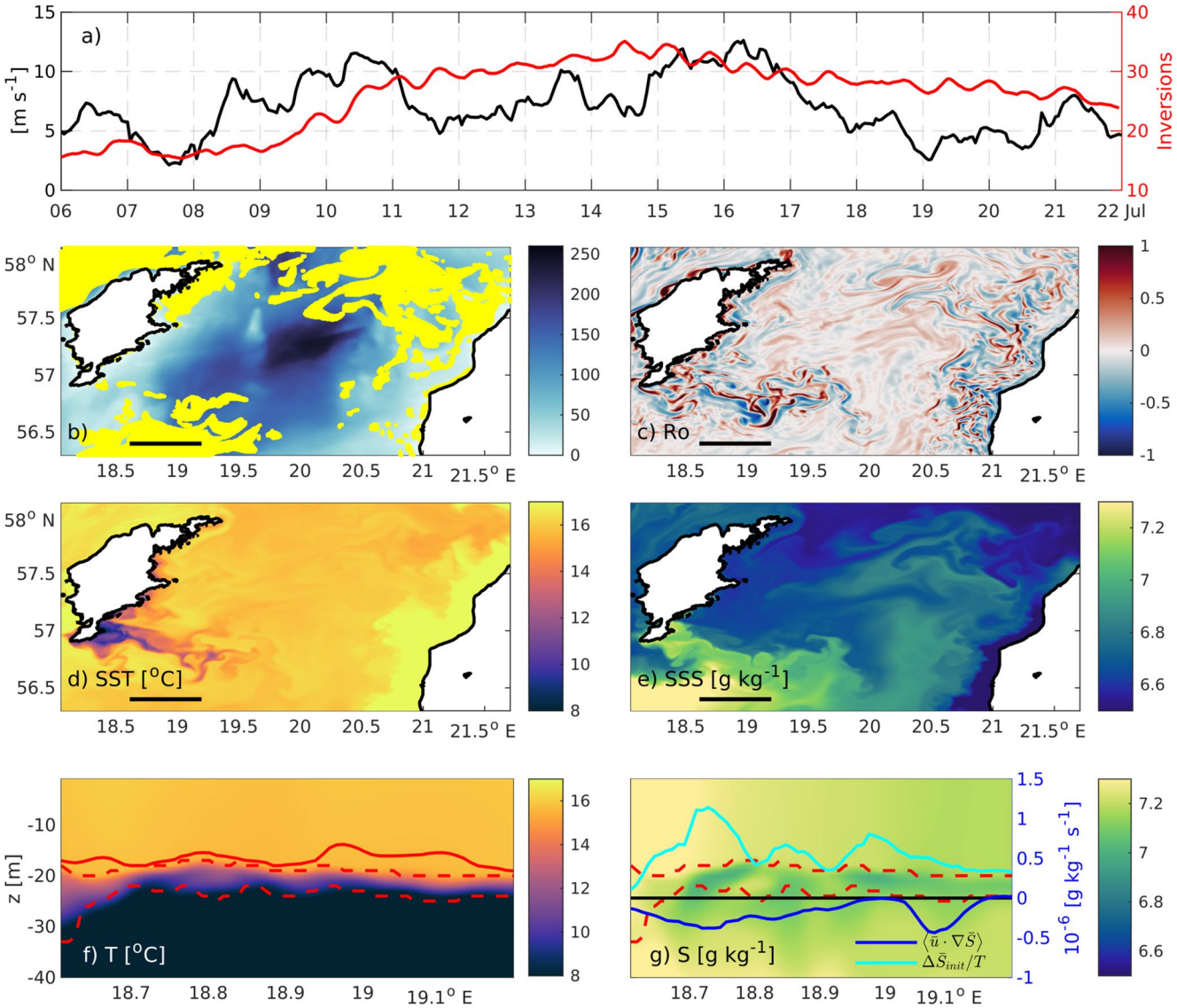

Figure 7. (a) Temporal evolution of the basin-averaged wind speed (left axis) vis-a-vis percentage of the inversions covering the study site (right axis). (b) Bathymetry of the study area along with the location of the salinity minima (yellow dots) as identified by the detection algorithm. (c) Rossby number, (d) sea surface temperature and, (e) surface salinity. Zonal transects of (f) temperature and (g) salinity along the black line shown in panels (b–e) respectively. The red line in (f) denotes the mixed layer depth, whereas the dashed lines in (f and g) delineate the thermocline region. The cyan and blue lines in panel (g) demonstrate the right-hand side (snapshot for 20 July 10:00 UTC) of Equation 6 and the left-hand side (daily average from 20 to 21 July 22:00 UTC) respectively. Panels (b–g) are snapshots from the model at the end of the study period, on 20 July 10:00 UTC.

At the end of the study period (Figure 7), the cold surface waters near the island of Gotland, indicating the upwelling process, extend offshore due to the preceding southwesterly wind episode. The initially low Ro numbers approach values of $\mathcal{O}(1)$ as strong submesoscale fronts and filaments emerge in the upwelling region (Figure 7c). The upwelling signal, visible also in the surface salinity, is disturbed by a saltier water mass that enters the basin from the southwest as it is advected by the wind (Figure 7e). A vertical section along this area indicates distinct salinity minima with a patchy distribution that extend across a distance of ~50 km (Figure 7g). The Movie S1 in Supporting Information S1 clearly shows that these minima are formed as the saltier waters move on top of the older and less saline waters through Ekman transport, providing evidence for the importance of advection in the generation of the thermocline salinity minima, as hypothesized in Section 3.

Application of the detection algorithm described in Section 3 reveals that such salinity minima are ubiquitous in the entire basin before and after the wind event (yellow dots in Figures 6b and 7b, and Movie S1 in Supporting

Information S1). The spatial distribution of these salinity minima is strongly correlated with the occurrence of lateral surface salinity gradients; more inversions occur at the northern part of the basin where the cold-fresh water masses meet the more saline ones. Salinity anomalies are also visible in the upwelling area, where strong submesoscale filaments appear (Figures 7b and 7c). Comparison of panels (b and g) of both Figures 6 and 7 shows that the inversions observed in the corresponding salinity transects are reliably identified by our detection algorithm. More inversions appear at the end of the study period (Figure 7b) compared to the beginning (Figure 6b). This is highlighted in Figure 7a (red line), showing the fraction of the domain (Eastern Gotland Basin) occupied by inversions. While only 15% of the domain is occupied by salinity minima in the first days, this portion strongly increases (∼30%) toward the end. Interestingly, the inversion abundance tends to follow the wind trend (with a time lag), increasing substantially during the strong southwesterly wind episode (9–11 July) and peaking on ∼14 July. An animation provided in Movie S1 in Supporting Information S1 shows further evidence of the enhancement of the inversions (see panel a) during the strong southwesterly winds (panel b). Note here that much stronger winds are expected to mix down the water column, thus destroying the salinity minima. Inspection of Figure 7g (cyan and blue lines) clearly shows that the condition for salinity minima, as derived in Equation 6, is fulfilled throughout the entire section. The observed positive $\Delta\bar{S}_{init}/T$ values verify the presence of new, freshly formed inversions, visible also from the colorscale. In contrast, the stronger $\Delta\bar{S}_{init}/T$ values translate to stronger inversions (e.g., around 18.75°E).

We conducted additional analyses to investigate the validity of the theoretical framework introduced in Section 3, focusing on the period with pronounced winds when salinity anomalies increase substantially. Figure 8a shows that the simulated magnitude of vertical salinity difference $\Delta\bar{S} \sim 0.2$–0.3 g kg^{-1} at the inversion locations (positive values) is consistent with the observations (Figure 1d). Salinity minima are abundant in the area, apart from the central basin and the coastal regions, as also evidenced by Figure 8b showing only the $\Delta\bar{S} > 0$ occurrences. To evaluate our hypothesis that inversions emerge primarily as a consequence of wind-induced differential advection, the left and right-hand sides of Equation 5 are shown in Figures 8a and 8c, respectively. Aside from small local discrepancies in the intensity of the values, a significant spatial resemblance exists between $\Delta\bar{S}$ and $\Delta\bar{S}_{init} - T\left\langle \bar{\boldsymbol{u}} \cdot \nabla\bar{S} \right\rangle$, as evidenced also by the correlation coefficient value of $r = 0.73$, which is high, considering that all other dynamical processes except horizontal advection are ignored in the diagnostics. The condition for salinity inversions (Equation 6; Figure 8e), as introduced in Section 3, is satisfied at almost all locations where salinity minima appear (Figure 8b). To further test our theory, a map including only the newly generated inversions is shown in Figure 8d. These inversions arise when the old inversions, formed prior to 12 July 11:00 UTC, are completely excluded from the results. Figure 8f shows that Equation 6 is valid in most sites where freshly formed inversions appear. This indicates that differential advection is, to a large extent, instrumental in generating inversions.

By considering three different domains, that is, one where inversions occur, one with only the freshly formed inversions, and finally a domain without inversions, we can estimate the percentages where Equation 6 is satisfied. We find that Equation 6 is fulfilled for: 76% of the domain covered by inversions, 58% when only the fresh inversions are included (true positive), whereas only 15% of the rest of the domain (true negative) satisfies Equation 6. Note here that Equation 6 is not satisfied in 22% of the domain covered by inversions (false negative; the remaining ∼2% comprises well-mixed waters where the detection algorithm fails since the ML cannot be defined). In these regions, the generation of the salinity minima is likely driven by other secondary dynamics. We will explore those potential secondary mechanisms in a subsequent manuscript, utilizing the observations collected during the field campaign.

5. Conclusions and Discussion

Previous studies have shown that thermocline temperature and salinity inversions can be triggered by a wealth of complex processes, including frontal subduction, mesoscale and submesoscale eddy stirring, and thermohaline interleaving (Hosegood et al., 2013; Pietri et al., 2013; Ruddick & Richards, 2003). Here, we identified Ekman-driven differential advection of surface waters above a stagnant thermocline as a simple yet efficient mechanism generating thermocline salinity inversions in a region with pronounced frontal gradients (see Figure 5). As the only ingredient required for this process to be effective is a component of the Ekman transport aligned with a frontal gradient, this process is likely to provide a relevant contribution to the formation of compensated

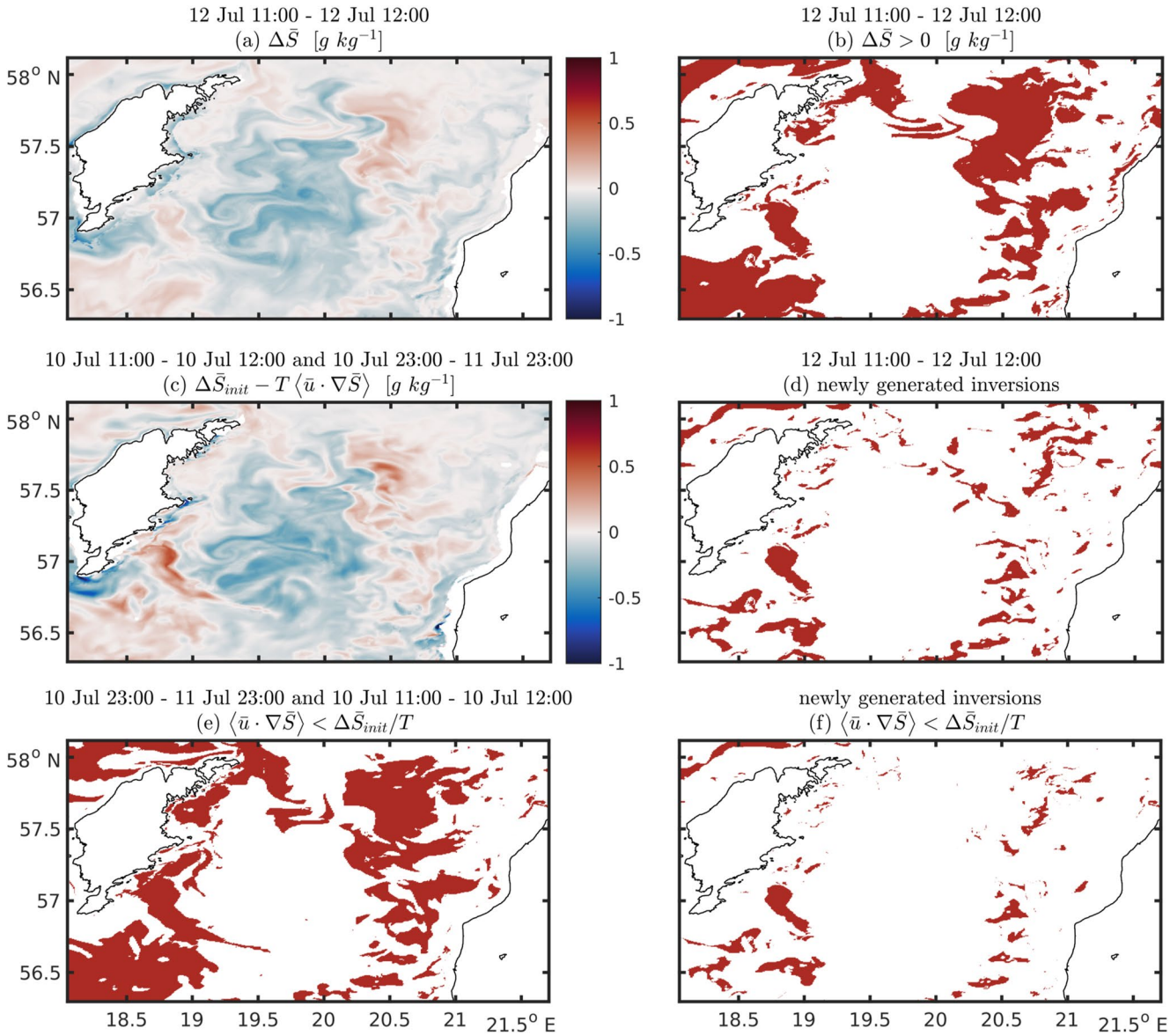

Figure 8. (a) Left-hand side term of Equation 5, denoting the vertical difference between the mixed layer salinity and the thermocline salinity. Positive values indicate the salinity minima sites. (b) Salinity minima locations, (c) right-hand side term of Equation 5 for comparison with panel (a), (d) regions covered by newly generated inversions, (e) regions satisfying the condition for inversions, and (f) regions of freshly generated minima where the condition for inversions is satisfied. The corresponding dates and integration intervals are shown on top of each panel. Note here that since the inversions are assumed to arise as a consequence of wind-driven advection acting half a day before, the dates are different in each panel.

thermocline T/S anomalies in many parts of the ocean. More specifically, thermocline salinity minima can arise globally during summer in regions with shallow MLs whenever lateral salinity gradients are favorably aligned to the Ekman transport.

Although Burchard et al. (2017) related these inversions to episodic upwelling events, our analysis indicates that they are a more general feature, emerging locally in the presence of strong surface salinity gradients while increasing with wind speeds (see Figure 7a and Movie S1 in Supporting Information S1). Yet, a time lag in the wind speed should be considered for their emergence since inversions are assumed to arise due to wind-driven advection acting almost half a day before. Vice-versa, their destruction, and decay by the wind field is also a plausible scenario when the wind becomes strong enough to mix down the water column. Focusing on the region of the inversions, stable stratification is preserved, at least temporarily, regardless of the reduction in salinity. The temperature gradients stabilize the water column as the minima stay confined inside the thermocline region.

The strong thermal stratification during summer, which is instrumental for our theory, makes the salinity behave almost as a passive tracer, affecting the density only weakly.

Considering that salinity is inert, the emergence and maintenance of salinity inversions may be indicative of weak lateral and vertical mixing as noted by Burchard et al. (2017). From a biogeochemistry perspective, inversions can represent waters with different biogeochemical properties. Moreover, since salinity inversions are primarily generated due to wind-driven differential advection, they can serve as indicators of past events of relatively strong Ekman dynamics. Beyond their role as a measure for Ekman transport, they are also important for preconditioning the effectiveness of mixing during wind- or convectively-driven events by generating vertical gradients that will be subsequently eroded. As shown by Chrysagi et al. (2021), the impact of Ekman-induced mixed-layer restratification on near-surface mixing is complex and ambivalent. If restratification is strong, it will create a layer that suppresses near-surface turbulence (see Carpenter et al., 2020). However, weaker surface-layer restratification will increase the mixing efficiency, which may lead to a net increase in mixing even if turbulence is slightly suppressed (see Figure 12 in Chrysagi et al., 2021). That would also affect the mixing of the biogeochemical gradients. In the upwelling area, inversions may also constitute a measure of the upwelling and the submesoscale filaments (e.g., Figure 7 and Movie S1 in Supporting Information S1). Salinity minima may also contribute indirectly to mixing by generating the necessary conditions for double diffusion.

The generation mechanism, presented in Section 3, resembles one of the mechanisms by which barrier layers (BLs) are formed (see Cronin & McPhaden, 2002). BLs are salinity-stratified isothermal layers bounded between the base of the ML and the top of the thermocline (Cronin & McPhaden, 2002). They act as barriers to turbulent mixing, isolating the deep cold water from the surface, and in some cases, they can even support temperature inversions (Cronin & McPhaden, 2002; de Boyer Montégut et al., 2007; Echols & Riser, 2020). Although our study focuses on thermocline salinity minima rather than regions with stable salinity stratification above the thermocline that characterize BLs, some of the potential generation mechanisms are similar. As shown in Cronin and McPhaden (2002), and similar to our study, frontal tilting is one of the potential mechanisms by which BLs could be formed. More specifically, a BL can be generated by differential advection, that is, the interaction of a vertical shear with a lateral salinity gradient. The dynamics and significance of those features in the Baltic Sea could be the subject of future work.

Other aforementioned dynamical mechanisms can also trigger salinity inversions; in this study, they are responsible for ∼20% of the inversions that differential advection fails to explain. This percentage may, however, be different in nature since processes such as the submesoscales that are known to trigger inversions (Hosegood et al., 2013; Pietri et al., 2013) are only marginally resolved by the numerical model. Frontal subduction that has been inferred to drive intense thermohaline and biogeochemical fluxes in other regions (Shcherbina et al., 2010; Thomsen et al., 2016) is expected to be relevant, in our study, mainly in the upwelling area when submesoscales arise. Oxygen observations (not shown) collected further offshore of the upwelling region indicate no significant relation between the salinity minima and oxygen. This can be due to the fact that here the surface layer properties are modified by advection rather than intrusion of a different water mass into the thermocline, as suggested by the aforementioned studies. Nonetheless, this would have different implications for the interpretation of water mass properties and composition.

Data Availability Statement

The data that support the findings of this study are openly available at http://doi.io-warnemuende.de/10.12754/data-2022-0001.

Acknowledgments
This paper contributes to the Collaborative Research Centre TRR 181 project on Energy Transfer in Atmosphere and Ocean, funded by the German Research Foundation (DFG), project 274762653. The authors are grateful to Peter Holtermann and to the two anonymous reviewers for their insightful comments and constructive suggestions. The authors acknowledge the North-German Supercomputing Alliance (HLRN) for providing HPC resources that have contributed to the research results reported in this manuscript.

References

Armstrong, D., Mitchell-Innes, B., Verheye-Dua, F., Waldron, H., & Hutchings, L. (1987). Physical and biological features across an upwelling front in the southern Benguela. *South African Journal of Marine Science*, *5*(1), 171–190. https://doi.org/10.2989/025776187784522559

Burchard, H., Basdurak, N. B., Gräwe, U., Knoll, M., Mohrholz, V., & Müller, S. (2017). Salinity inversions in the thermocline under upwelling favorable winds. *Geophysical Research Letters*, *44*(3), 1422–1428. https://doi.org/10.1002/2016GL072101

Burchard, H., & Beckers, J. M. (2004). Non-uniform adaptive vertical grids in one-dimensional numerical ocean models. *Ocean Modeling*, *6*(1), 51–81. https://doi.org/10.1016/S1463-5003(02)00060-4

Burchard, H., & Bolding, K. (2002). GETM: A general estuarine transport model, (Vol. *157*). Tech. Rep. EUR 20253 EN, Eur. Comm.

Carpenter, J. R., Rodrigues, A., Schultze, L. K. P., Merckelbach, L. M., Suzuki, N., Baschek, B., & Umlauf, L. (2020). Shear instability and turbulence within a submesoscale front following a storm. *Geophysical Research Letters*, *47*(23). https://doi.org/10.1029/2020GL090365

Chrysagi, E., Umlauf, L., Holtermann, P., Klingbeil, K., & Burchard, H. (2021). High-resolution simulations of submesoscale processes in the Baltic Sea: The role of storm events. *Journal of Geophysical Research: Oceans*, *126*(3), e2020JC016411. https://doi.org/10.1029/2020JC016411

Chu, P. C., & Fan, C. (2019). Global ocean synoptic thermocline gradient, isothermal-layer depth, and other upper ocean parameters. *Scientific Data*, *6*(1), 1–10. https://doi.org/10.1038/s41597-019-0125-3

Cronin, M. F., & McPhaden, M. J. (2002). Barrier layer formation during westerly wind bursts. *Journal of Geophysical Research: Oceans*, *107*(C12), SRF21-1–SRF21-12. https://doi.org/10.1029/2001JC001171

de Boyer Montégut, C., Madec, G., Fischer, A. S., Lazar, A., & Iudicone, D. (2004). Mixed layer depth over the global ocean: An examination of profile data and a profile-based climatology. *Journal of Geophysical Research C: Oceans*, *109*, C12003. https://doi.org/10.1029/2004JC002378

de Boyer Montégut, C., Mignot, J., Lazar, A., & Cravatte, S. (2007). Control of salinity on the mixed layer depth in the world ocean: 1. General description. *Journal of Geophysical Research: Oceans*, *112*(C6). https://doi.org/10.1029/2006JC003953

Echols, R., & Riser, S. C. (2020). Spice and barrier layers: An Arabian Sea case study. *Journal of Physical Oceanography*, *50*(3), 695–714. https://doi.org/10.1175/JPO-D-19-0215.1

Fennel, W., Radtke, H., Schmidt, M., & Neumann, T. (2010). Transient upwelling in the central Baltic Sea. *Continental Shelf Research*, *30*(19), 2015–2026. https://doi.org/10.1016/j.csr.2010.10.002

Galperin, B., Kantha, L. H., Hassid, S., & Rosati, A. (1988). A quasi-equilibrium turbulent energy model for geophysical flows. *Journal of the Atmospheric Sciences*, *45*(1), 55–62. https://doi.org/10.1175/1520-0469(1988)045⟨0055:AQETEM⟩2.0.CO;2

Gräwe, U., Klingbeil, K., Kelln, J., & Dangendorf, S. (2019). Decomposing mean sea level rise in a semi-enclosed basin, the Baltic Sea. *Journal of Climate*, *32*(11), 3089–3108. https://doi.org/10.1175/JCLI-D-18-0174.1

Hofmeister, R., Burchard, H., & Beckers, J. M. (2010). Non-uniform adaptive vertical grids for 3D numerical ocean models. *Ocean Modeling*, *33*(1–2), 70–86. https://doi.org/10.1016/j.ocemod.2009.12.003

Holtermann, P. L., Burchard, H., Grawe, U., Klingbeil, K., & Umlauf, L. (2014). Deep-water dynamics and boundary mixing in a nontidal stratified basin: A modeling study of the Baltic Sea. *Journal of Geophysical Research: Oceans*, (2), 3134–3157. https://doi.org/10.1002/2013jc009483

Hosegood, P. J., Gregg, M. C., & Alford, M. H. (2013). Wind-driven submesoscale subduction at the North Pacific Subtropical Front. *Journal of Geophysical Research: Oceans*, *118*(10), 5333–5352. https://doi.org/10.1002/jgrc.20385

Kuzmina, N., Rudels, B., Stipa, T., & Zhurbas, V. (2005). The structure and driving mechanisms of the Baltic intrusions. *Journal of Physical Oceanography*, *35*(6), 1120–1137. https://doi.org/10.1175/JPO2749.1

Lass, H. U., Mohrholz, V., Nausch, G., & Siegel, H. (2010). On phosphate pumping into the surface layer of the eastern Gotland Basin by upwelling. *Journal of Marine Systems*, *80*(1–2), 71–89. https://doi.org/10.1016/j.jmarsys.2009.10.002

Lips, U., Kikas, V., Liblik, T., & Lips, I. (2016). Multi-sensor in situ observations to resolve the submesoscale features in the stratified Gulf of Finland, Baltic Sea. *Ocean Science*, *12*(3), 715–732. https://doi.org/10.5194/os-12-715-2016

Onken, R., Baschek, B., & Angel-Benavides, I. M. (2020). Very high-resolution modeling of submesoscale turbulent patterns and processes in the Baltic Sea. *Ocean Science*, *16*(3), 657–684. https://doi.org/10.5194/os-16-657-2020

Pietri, A., Testor, P., Echevin, V., Chaigneau, A., Mortier, L., Eldin, G., & Grados, C. (2013). Finescale vertical structure of the upwelling system off southern Peru as observed from glider data. *Journal of Physical Oceanography*, *43*(3), 631–646. https://doi.org/10.1175/JPO-D-12-035.1

Roden, G. I. (1964). Shallow temperature inversions in the Pacific Ocean. *Journal of Geophysical Research*, *69*(14), 2899–2914. https://doi.org/10.1029/JZ069i014p02899

Ruddick, B., & Richards, K. (2003). Oceanic thermohaline intrusions: Observations. *Progress in Oceanography*, *56*(3), 499–527. https://doi.org/10.1016/S0079-6611(03)00028-4

Saha, S., Moorthi, S., Pan, H.-L., Wu, X., Wang, J., Nadiga, S., et al. (2010). The NCEP climate forecast system reanalysis. *Bulletin of the American Meteorological Society*, *91*(8), 1015–1058. https://doi.org/10.1175/2010BAMS3001.1

Shcherbina, A. Y., Gregg, M. C., Alford, M. H., & Harcourt, R. R. (2010). Three-dimensional structure and temporal evolution of submesoscale thermohaline intrusions in the North Pacific Subtropical Frontal Zone. *Journal of Physical Oceanography*, *40*(8), 1669–1689. https://doi.org/10.1175/2010JPO4373.1

Smagorinsky, J. (1963). General circulation experiments with the primitive equations. *Monthly Weather Review*, *91*(3), 99–164. https://doi.org/10.1175/1520-0493(1963)091⟨0099:GCEWTP⟩2.3.CO;2

Smith, K. S., & Ferrari, R. (2009). The production and dissipation of compensated thermohaline variance by mesoscale stirring. *Journal of Physical Oceanography*, *39*(10), 2477–2501. https://doi.org/10.1175/2009JPO4103.1

Stommel, H., & Fedorov, K. N. (1967). Small-scale structure in temperature and salinity near Timor and Mindanao. *Tellus*, *19*(2), 306–325. https://doi.org/10.3402/tellusa.v19i2.9792

Thomas, L. N., & Lee, C. M. (2005). Intensification of ocean fronts by down-front winds. *Journal of Physical Oceanography*, *35*(6), 1086–1102. https://doi.org/10.1175/JPO2737.1

Thomsen, S., Kanzow, T., Colas, F., Echevin, V., Krahmann, G., & Engel, A. (2016). Do submesoscale frontal processes ventilate the oxygen minimum zone off Peru? *Geophysical Research Letters*, *43*(15), 8133–8142. https://doi.org/10.1002/2016GL070548

Ueno, H., Oka, E., Suga, T., Onishi, H., & Roemmich, D. (2007). Formation and variation of temperature inversions in the eastern subarctic North Pacific. *Geophysical Research Letters*, *34*(5). https://doi.org/10.1029/2006GL028715

Umlauf, L., & Burchard, H. (2005). Second-order turbulence models for geophysical boundary layers. A review of recent work. *Continental Shelf Research*, *25*, 795–827. https://doi.org/10.1016/j.csr.2004.08.004

Woods, J. D., Onken, R., & Fischer, J. (1986). Thermohaline intrusions created isopycnically at oceanic fronts are inclined to isopycnals. *Nature*, *322*(6078), 446–449. https://doi.org/10.1038/322446a0